Extremely nonlinear Raman interaction of an ultrashort nitrogen ion laser with an impulsively excited molecular wave packet

Zhaoxiang Liu,[1,3] Jinping Yao,[1,*] Haisu Zhang,[2,†] Bo Xu,[1,3] Jinming Chen,[1,3,4] Fangbo Zhang,[1,3] Zhihao Zhang,[1,3,4] Yuexin Wan,[1,3] Wei Chu,[1] Zhenhua Wang,[2] and Ya Cheng[1,2,5,6,‡]

[1]*State Key Laboratory of High Field Laser Physics, Shanghai Institute of Optics and Fine Mechanics, Chinese Academy of Sciences, Shanghai 201800, China*

[2]*State Key Laboratory of Precision Spectroscopy, East China Normal University, Shanghai 200062, China*

[3]*University of Chinese Academy of Sciences, Beijing 100049, China*

[4]*School of Physical Science and Technology, ShanghaiTech University, Shanghai 200031, China*

[5]*Collaborative Innovation Center of Extreme Optics, Shanxi University, Taiyuan, Shanxi 030006, China*

[6]*Collaborative Innovation Center of Light Manipulations and Applications, Shandong Normal University, Jinan 250358, China*

(Received 29 October 2019; accepted 13 March 2020; published 13 April 2020)

We report on the generation of cascaded rotational Raman scattering up to 58th order in coherently excited CO_2 molecules. Raman scattering with more than 600 sidebands is obtained using an intense femtosecond laser to impulsively excite rotational coherence and femtosecond-laser-induced N_2^+ lasing to generate cascaded Raman signals. This configuration allows this experiment to be performed with a single femtosecond laser beam at free-space standoff locations. It is revealed that the efficient spectral extension of Raman signals is attributed to the specific structures of N_2^+ lasing in the spectral and temporal domains and the ideal spatial overlap of the femtosecond laser and N_2^+ lasing. A Raman spectrum extending above 2000 cm^{-1} naturally corresponds to a femtosecond pulse train due to the periodic revivals of molecular rotational wave packets.

DOI: 10.1103/PhysRevA.101.043404

Synthesizing femtosecond and subfemtosecond pulses by molecular modulators has been well established in recent decades [1–4]. The concerted vibration or rotation of molecules can efficiently modulate the optical polarizability of the medium and generate high-order Raman scattering with a broad spectral range. Octave-spanning spectra with good phase coherence are routinely generated through molecular modulators with external guiding structures such as hollow-core capillaries and photonic crystal fibers [1,5,6]. This necessitates a convenient dispersion compensation for ultrashort-pulse generation. Molecular modulators not only feature a broader bandwidth as compared to the usual optoelectronic modulators [7,8], but also have a higher conversion efficiency than attosecond pulses generated by high-order harmonic generation [9]. Depending on the Raman frequencies of molecules and the duration of the input pulse, both isolated ultrashort-pulse and periodic ultrashort-pulse trains are generated by adiabatically and/or impulsively prepared molecular modulators [10–13]. Therefore, it holds numerous demanding applications in time-resolved chemistry, optical communications, precision metrology, or spectroscopy, to cite a few.

On the other hand, laser-induced molecular alignment has increased interest due the compelling need to manipulate the orientation of the molecular axis during diverse physical processes and technological applications. In the nonadiabatic regime, broad coherent rotational wave packets are generated in molecules kicked by moderately intense ultrashort laser pulses [14], which manifest themselves as a postpulse field-free molecular alignment with periodic revivals. The periodic revivals of the rotational wave packets of constituent molecules will induce an ultrafast modulation of the refractive index, which will substantially affect the propagation of time-delayed pulses. This effect has been widely employed to control and localize an incident light pulse both in the spatial and temporal dimensions [12,15,16].

In this article, we observed high-order rotational Raman signals extending above 2000 cm^{-1} in impulsively excited CO_2 molecules, which are composed of more than 600 Raman sidebands. A single femtosecond pump laser is utilized to generate N_2^+ lasing as well as rotational wave packets in CO_2 molecules, which combines the advantages of the impulsive preparation of molecular wave packets with a broadband pump and high spectral resolution with a narrow-bandwidth probe. In particular, N_2^+ lasing served as an ideal light source to generate cascaded Raman scattering in impulsively excited molecules, due to the natural spatial overlap of the lasing radiation with the pump laser. Moreover, the inherent structures of free-space N_2^+ lasing in the spectral and temporal domains favor a high spectral resolution to discriminate individual rotational states and an optimized sampling window of molecular Raman responses [17,18]. Specifically, the asymmetric temporal profile of an N_2^+ lasing pulse with a fast-rising edge and a slow-trailing edge (as revealed later) is highly desired in fs/ps coherent anti-Stokes Raman scattering

*jinpingmrg@163.com
†hszhang@phy.ecnu.edu.cn
‡ya.cheng@siom.ac.cn

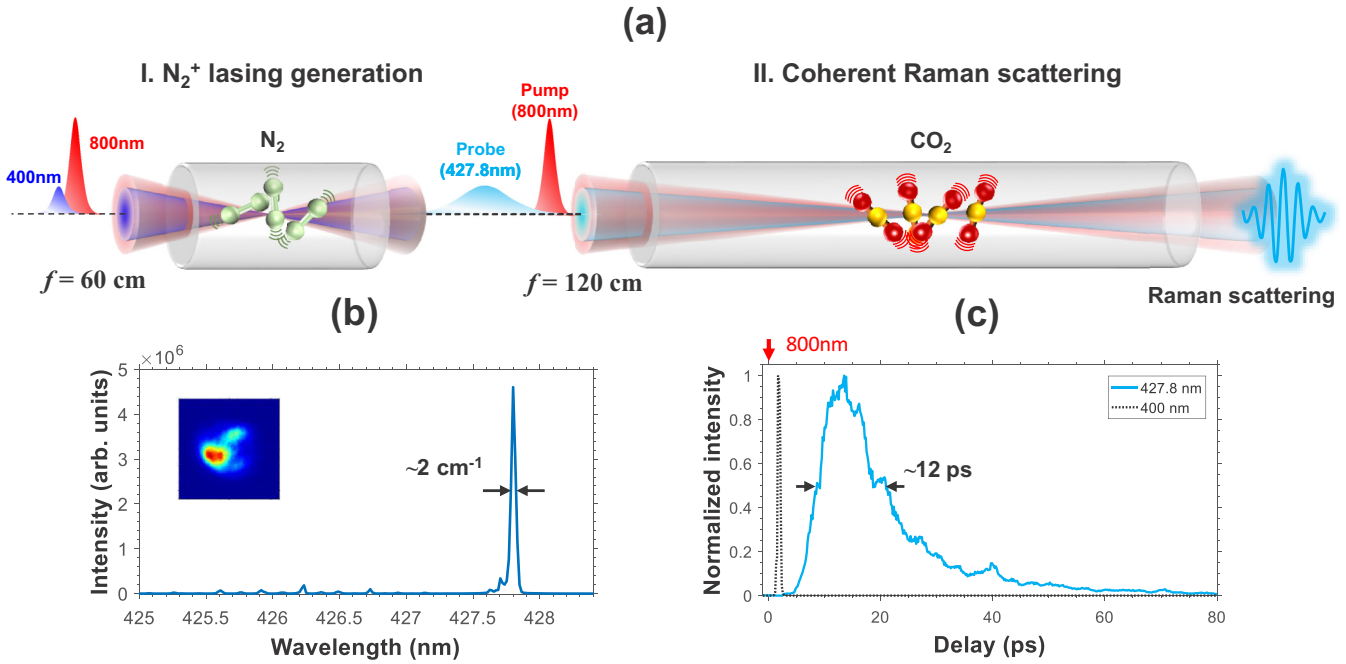

FIG. 1. (a) Schematic of the experimental setup for N_2^+ lasing generation and coherent Raman scattering. (b) The measured spectrum of N_2^+ lasing and its spatial profile (inset). (c) The temporal information of N_2^+ lasing (blue solid line) and the 400-nm laser pulses (black dot line) obtained by the cross-correlation technique. In this measurement, the sum frequency of the N_2^+ lasing signal or the 400-nm pulses and a weak 800-nm pulse in a BBO crystal is recorded as a function of the delay. The zero delay is defined as the moment when the 800-nm pump laser arrives at the interaction region in the second chamber, as indicated with a red arrow.

(CARS) spectroscopy for gas thermometry and combustion diagnosis [19]. Besides, the few-picosecond duration of N_2^+ lasing greatly mitigates the sensitivity of pump-probe delays and the group-velocity mismatch-induced walk-off between synchronized molecular rotations and the probe pulse. All of the above merits enable the observation of cascading rotational Raman scattering as high as the 58th order under free-space conditions. Although one lasing wavelength of N_2^+ (i.e., 427.8 nm) is selected in the current proof-of-principle experiment, the versatile wavelength tunability of N_2^+ lasing within the vibrational manifolds of N_2^+ electronic transition promises a broad spectral coverage for the attainable Raman spectrum with many closely spaced peaks.

The experiment was performed using a commercial Ti:sapphire laser system (Legend Elite-Duo, Coherent, Inc.), which delivers 800-nm, 40-fs laser pulses with a pulse energy of 6.2 mJ at a repetition rate of 1 kHz. The beam diameter was measured to be about 9 mm. As schematically illustrated in Fig. 1(a), the 800-nm laser beam was focused with an $f = 60$ cm lens into a static chamber filled with 15-mbar nitrogen gas. A 30-μm-thick beta barium borate (BBO) crystal was used to produce second-harmonic pulses with a central wavelength of ~400 nm. In the chamber, the intensity of the 800-nm pulse is measured to 5.9×10^{13} W/cm^2, whereas the 400-nm pulse is about two orders of magnitude weaker. The 400-nm pulse is about 0.3 ps after the 800-nm pulse due to dispersion of the BBO crystal and the front window of the chamber. Such a two-color laser field will induce a strong N_2^+ lasing radiation at a 427.8-nm wavelength, as previously reported [20,21]. All light signals exiting from the first chamber were collimated and then were focused by an $f = 120$ cm lens into the second chamber to generate the coherent Raman scattering of CO_2 molecules. We do not filter the 400-nm pulse between the first and second chamber. The focusing geometry and gas pressures in two chambers are independently optimized to obtain strong N_2^+ lasing radiation with a narrow spectrum and efficient Raman shifts. We chose CO_2 as the model target gas in the second chamber, because CO_2 molecules have a large cross section of rotational Raman scattering and a small rotational constant. The Raman scattering signal was completely collected by a lens into a grating spectrometer with a spectral resolution of 1.6 cm^{-1} (Shamrock 500i, Andor). Some filters were placed before the spectrometer to improve the signal-to-noise ratio.

In this experiment, the residual 800-nm laser from the first chamber was used as the pump beam, which impulsively excites the rotational coherence of CO_2 molecules. Its intensity is estimated to be 1.9×10^{13} W/cm^2. The N_2^+ lasing radiation with an energy of ~0.5 nJ served as the probe beam, which will be inelastically scattered to generate Raman sidebands in coherently excited CO_2 molecules. As shown in Fig. 1(b), the lasing radiation at 427.8 nm has a spectral bandwidth of ~ 2 cm^{-1}, enabling the generation of a rotational-state-resolved Raman signal. We can also observe some discrete peaks on the blue side of the 427.8-nm lasing line, which correspond to R-branch rotational transitions from $B\,^2\Sigma_u^+(v' = 0)$ to $X\,^2\Sigma_g^+(v = 1)$ states. It should be emphasized that these R-branch signals are more than one order of magnitude weaker than the 427.8-nm radiation under our experimental conditions, as indicated in Fig. 1(b). Thus, their

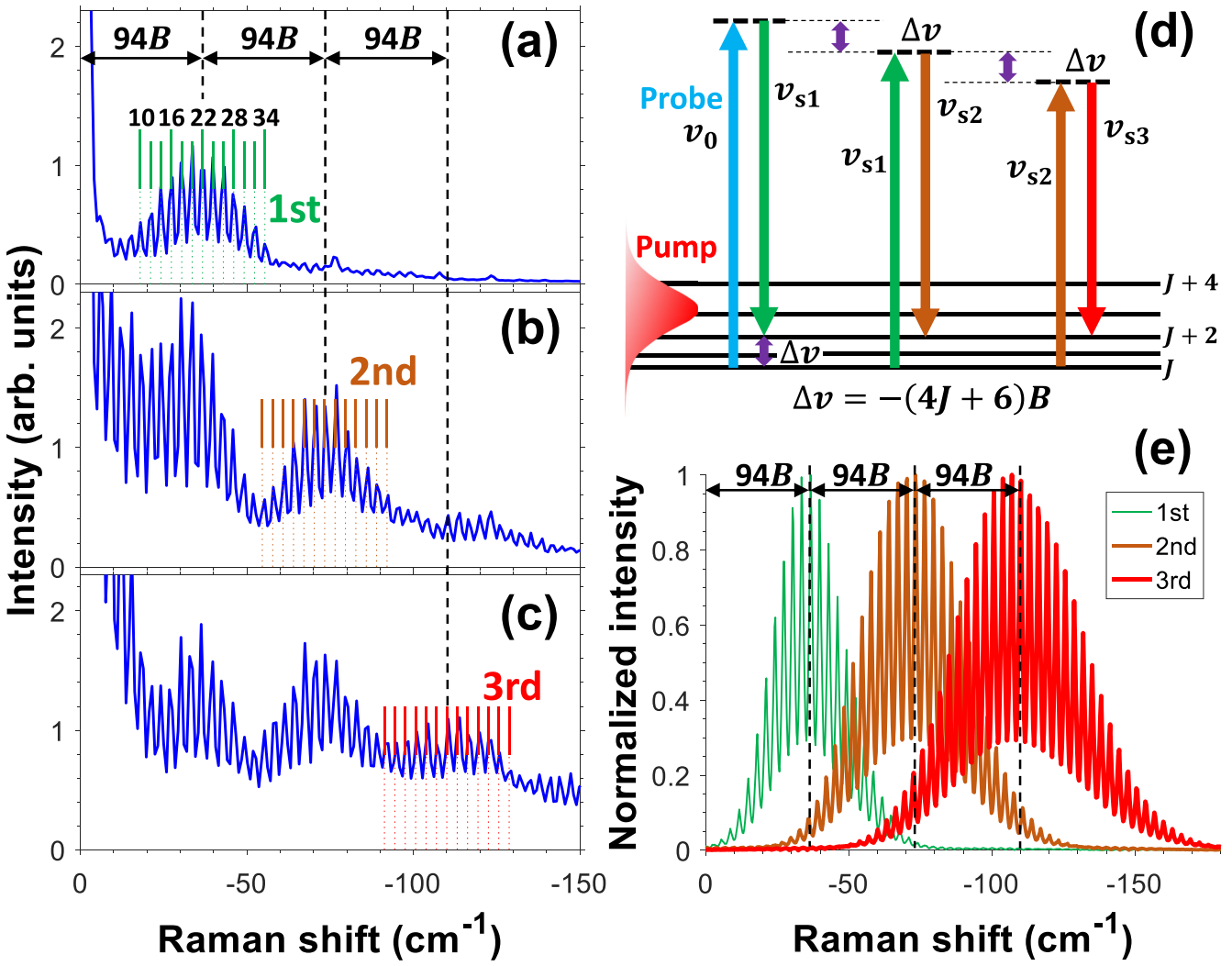

FIG. 2. Measured rotational Raman spectra (blue solid curves) at gas pressures of (a) 20 mbar, (b) 60 mbar, and (c) 120 mbar, respectively. The theoretically calculated Raman shifts are indicated by vertical lines. (d) Schematic diagram of the first-, second-, and third-order rotational Raman scattering. (e) Simulated Raman spectra for the first (left), second (middle) and third (right) order Raman scatterings. Each order Raman scattering is normalized independently.

Raman scattering signals are considered negligible. The N_2^+ lasing radiation also exhibits a good spatial profile and a small divergence angle of 6.2 mrad, allowing a good spatial overlap with the pump beam. The temporal profile of the lasing radiation is further illustrated in Fig. 1(c), featuring a few-picosecond rising edge and a long falling edge lasting dozens of picoseconds, as well as a 13-ps delay with respect to the 800-nm pump pulse. All these features are inherited from the coherent and superradiance nature of N_2^+ lasing as revealed by previous works [22,23]. It is noteworthy that the delay between N_2^+ lasing and the residual 800-nm pulse is determined by the initial delay of 800- and 400-nm pulses in the first chamber (~0.3 ps), the superradiance delay of N_2^+ lasing, and the dispersion of optical elements and gas. The efficiency of Raman scattering is robust for this delay due to the long pulse duration of N_2^+ lasing as well as the long rotational period of CO_2 molecules. Therefore, although we did not specially optimize the time delay between the 800-nm pulse and 427.8-nm lasing in the second chamber, their relative delay still enables efficient Raman scattering.

First, we captured the spectra of Raman scattering at different CO_2 gas pressures. A series of closely spaced peaks appears on two sides of the N_2^+ lasing line, corresponding to the Stokes and anti-Stokes Raman scattering processes. Here, we focus on the Stokes Raman lines lying on the long-wavelength side. The corresponding frequency shifts with respect to the N_2^+ lasing line are plotted in Figs. 2(a)–2(c). At a gas pressure of 20 mbar, as shown in Fig. 2(a), a Gaussian distribution of line intensities for the rotational Raman sidebands can be clearly observed with frequency shifts determined as $\Delta v = -(4J + 6)B$ (green vertical lines), where $B = 0.3902\,\mathrm{cm}^{-1}$ is the rotational constant for CO_2 molecules in the ground state and J is the rotational quantum number [24]. The J values corresponding to Raman transitions from J to $J + 2$ are indicated above the vertical lines in Fig. 2(a). Since only even J states are populated for CO_2 molecules, the frequency difference between adjacent Raman peaks is a constant value

of $8B$ (i.e., $\sim 3.1\,\mathrm{cm}^{-1}$), except for the frequency shift of $6B$ corresponding to a Raman transition from $J = 0$ to $J = 2$. Raman scattering from N_2 molecules is negligible owing to its smaller Raman cross section and shorter medium length as compared to CO_2 molecules.

With the increase of CO_2 gas pressures, second and third bands with larger Raman shifts appear, which correspond to second- and third-order rotational Raman scattering, respectively. These high-order Raman scattering signals are generated through cascaded processes, which are schematically illustrated in Fig. 2(d). First-order Raman scattering produces a series of Stokes Raman peaks due to the populated multiple rotational states, as observed in Fig. 2(a). Each sideband within the first-order Raman scattering can act as a new pump source and be further scattered from different initial rotational states to generate multiple second-order Stokes components. As a result, the number of Raman sidebands grows with the Raman order. The cascading process is quite efficient due to the prepared rotational coherence by the broadband pump laser.

Figure 2(e) shows the theoretically calculated spectra of first-, second-, and third-order Raman scattering. The third-order polarization to describe the coherent Stokes Raman scattering is given by [25,26]

$$P^{(3)}(t-\tau) = \left(\frac{i}{\hbar}\right)^3 A_0(t-\tau)\left[\int_0^\infty dt_2 R(t_2)|A_1(t-t_2)|^2\right], \tag{1}$$

where A_1 and A_0 are the electric field envelopes of the pump (800-nm laser) and probe (427.8-nm lasing) pulses, respectively. The pump field has a 40-fs Gaussian envelope, and the envelope of the probe field is taken as the measured curve in Fig. 1(c). The pump-probe delay τ is fixed at 13 ps. The response function is given by $R(t_2) = \sum_J a_{JJ'}(T)\exp(i\Delta\Omega_{JJ'}t_2)$ with the frequency difference between J and J' ($J' = J+2$) states $\Delta\Omega_{JJ'}(<0)$. This term $a_{JJ'}(T)$ is calculated by $a_{JJ'}(T) = \frac{4}{45}\frac{N}{\hbar}\gamma^2 b_{JJ'}\Delta\rho_{JJ'}(T)F(J)$ with the temperature $T = 294\,\mathrm{K}$, the number density N, the Placzek-Teller coefficient $b_{JJ'}$, the polarization anisotropy γ, and the correction term for centrifugal distortion $F(J)$. $\Delta\rho_{JJ'}(T)$ is the normalized population difference between J and J' states, which is expressed as $\Delta\rho_{JJ'}(T) = \frac{g_J(2J+1)}{Q_J}\{\exp[-\frac{hcBJ(J+1)}{kT}] - \exp[-\frac{hcBJ'(J'+1)}{kT}]\}$ with the statistical weight factor g_J, the (parity separated) partition function Q_J, the rotational constant $B = 0.3902\,\mathrm{cm}^{-1}$, and Boltzmann's constant k [27]. Theoretically, the first-order Raman spectrum is obtained by $|\int P^{(3)}(t-\tau)\exp(-i\omega t)dt|^2$, which is shown with the green line (left) in Fig. 2(e). The first-order Raman signal A_{s1}, which is calculated by Eq. (1), serves as a new probe field to generate the second-order Raman scattering. By replacing A_0 with A_{s1} in Eq. (1), we can obtain the second-order Raman spectrum, as shown with the brown line (middle) in Fig. 2(e). Similarly, the the third-order Raman spectrum is obtained with the second-order Raman signal A_{s2} as a new probe source. Such a theoretical treatment not only emphasizes the cascaded nature of high-order Raman scattering but also enables a clear demonstration of the spectral characteristics for each order Raman scattering.

The calculated frequency shifts for second- and third-order Raman scattering are indicated with brown and red vertical lines in Figs. 2(b) and 2(c), respectively. The deviation between the theoretical and experimental values is smaller than the resolution of the spectrometer. The simulated spectra in Fig. 2(e) reproduce the main features of the experimental results. Similar to the first-order Raman scattering, the second- and third-order Raman scattering spectra also consist of a sequence of equally spaced peaks. For all Raman orders, the strongest Raman peak corresponds to the Raman scattering from $J = 22$ to $J = 24$, which is determined by the initial thermal distribution of molecules among the rotational states. Therefore, two adjacent Raman orders are separated by $94B$, as demonstrated experimentally and theoretically. In addition, Fig. 2(e) also clearly shows a broader bandwidth at a higher Raman order. A spectral overlap among different Raman orders will result in the generation of a flat structure in the total Raman spectrum, as observed in Fig. 2(c). Based on these spectral analyses, we confirmed the generation of high-order cascaded Raman scattering from CO_2 molecules.

When the CO_2 gas pressure is further increased, higher-order Raman signals are observed. As illustrated in Fig. 3, Raman scattering can be extended to 17th, 32th, 46th, and 58th orders at CO_2 gas pressures of 150 mbar, 300 mbar, 500 mbar, and 1 atm, respectively. Such a high-order cascaded Raman scattering process induces a frequency shift $>2000\,\mathrm{cm}^{-1}$ in the 1-atm CO_2 gas, where the conversion efficiency from N_2^+ lasing to all Raman sidebands is estimated to be about 9%. The Raman signal propagates along the direction of the pump laser with a divergence angle of 8.5 mrad. Its spatial profile in the far field is shown in the inset of Fig. 3. These spatial characteristics further demonstrate its nature of coherent Raman scattering. More interestingly, unlike most cascaded nonlinear processes, Raman signals do not show a sharp decay with the increase of Raman order. Instead, they exhibit a plateau in the high-order Raman spectra, which is particularly obvious at 1 atm. In addition, two strong spectral lines with frequency shifts of 1285 and $1388\,\mathrm{cm}^{-1}$ are overlaid on the rotational Raman spectra, which correspond to vibrational Raman scatterings of $02^00(\Sigma_g^+)$ and $10^00(\Sigma_g^+)$ states of CO_2 molecules, respectively [24].

Furthermore, we performed a cross-correlation measurement to obtain the temporal information of these Raman scattering signals. To this end, a weak 800-nm laser beam together with a Raman signal generated at 1 atm are launched into a BBO crystal to generate the time- and frequency-resolved sum frequency signal (SFS). After integrating spectrally, we can obtain the SFS as a function of the time delay of two beams, which approximately reflects the temporal structure of Raman scattering. As indicated by the red dotted-dashed line in Fig. 4, the Raman signal is composed of a pulse train with a constant interval of $\sim$10.7 ps, which approximately equals one quarter of the full rotational period of CO_2 molecules T_{rev}. The measured result clearly shows that strong Raman scattering only occurs at the revival moments of rotational wave packets. The relative intensity of these subpulses basically follows the temporal envelope of N_2^+ lasing. Therefore, a cascaded Raman spectrum can synthesize a femtosecond pulse train without any dispersion compensation. Previous studies show that both the pulse duration of N_2^+ lasing and its delay with respect to the 400-nm seed pulse (i.e., superradiance delay) strongly depend on the gas pressure [23]. Therefore, by simply

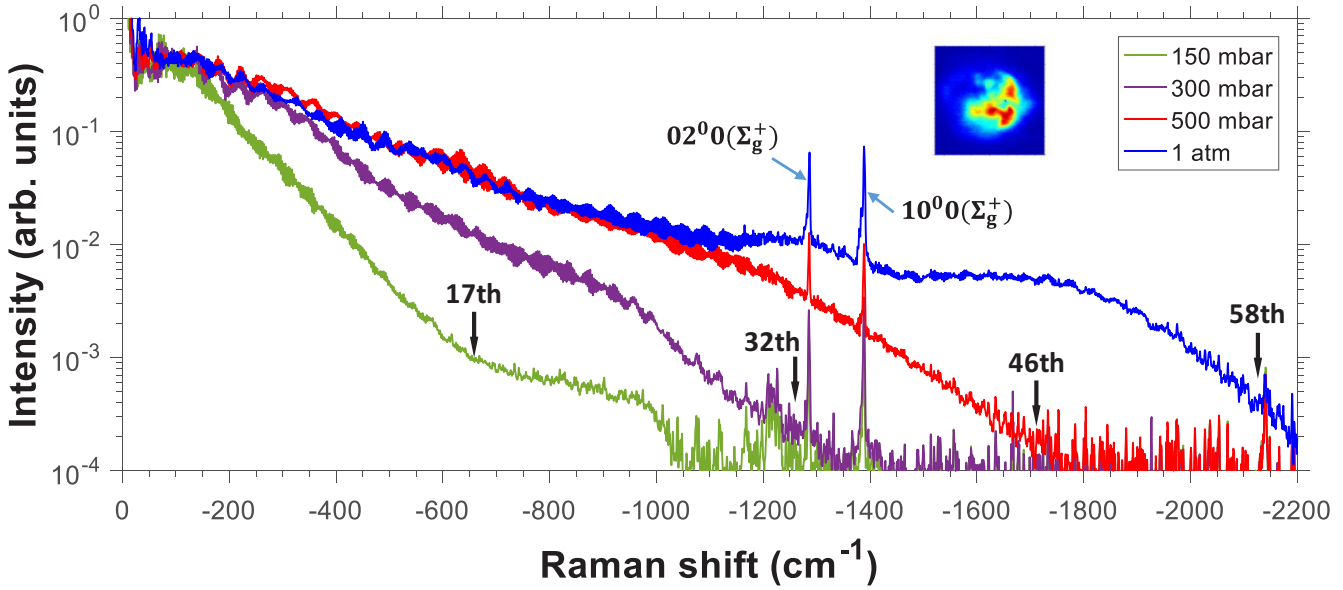

FIG. 3. Measured Raman spectra at the gas pressure of 150 mbar (green line), 300 mbar (purple line), 500 mbar (red line), and 1 atm (blue line), respectively. The inset shows the spatial profile of Raman signals at 1 atm.

adjusting the gas pressure in the lasing generation chamber, active control of the temporal profiles of N_2^+ lasing can be realized. It can be further used to engineer the high-order cascaded Raman spectrum as well as the temporal profile of the synthesized pulse.

The temporal structure of cascaded Raman scattering is easily understood in terms of refractive-index modulation. As shown in previous studies [12,15], an impulsive excitation of the rotational wave packets by a femtosecond pump laser will cause the ultrafast modulation of the refractive index. In our experiment, the ionization probability of CO_2 molecules is extremely low, and polarizations of the pump and probe laser fields are nearly parallel to each other. In this case, the time-independent refractive index $n(t)$ caused by the nondiabatic alignment of the pump laser is given by [12,15]

$$n(t) \approx 1 + \frac{N}{2\varepsilon_0}[\alpha_\perp + (\alpha_\parallel - \alpha_\perp)\langle\cos^2\theta(t)\rangle]. \quad (2)$$

Here, N is the number density of CO_2 molecules, $\alpha_\parallel$ ($\alpha_\perp$) is the parallel (perpendicular) component of the anisotropic polarizability, ε_0 is the dielectric constant, and $\langle\cos^2\theta(t)\rangle$ is the alignment factor determined by the pump field with θ being the angle of molecular axis with respect to the polarization direction of the pump laser. This formula shows that the molecular alignment of CO_2 is modulated during rotational revivals, which is imprinted on the refraction index. When the N_2^+ lasing signal is injected into the refractive-index modulated CO_2 molecules, its frequency will be shifted

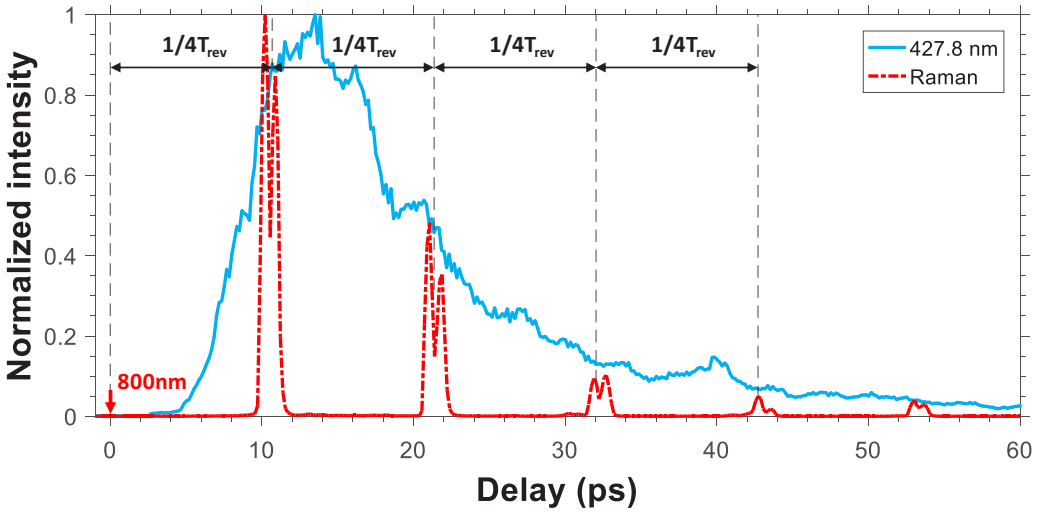

FIG. 4. Temporal structures of Raman signal at 1 atm (red dotted-dashed line) and N_2^+ lasing (blue solid line) measured with the cross-correlation technique.

to generate Raman sidebands. Since the modulation of the refraction index mainly occurs during rotational revivals, Raman scattering at these moments is most efficient. The temporal structure of rotational Raman scattering reveals the relatively simple phase relation between different Raman sidebands.

It should be emphasized that the observed high-order Raman scattering is achieved in free-space conditions, contrary to the usually utilized meter-scale gas-filled hollow-core fibers for efficient cascading Raman scattering generation in the nanosecond pumping scheme [5,6]. This is because the intense pump laser enables us to generate a channel of rotational quantum wave packets with a length much longer than the Rayleigh range. Furthermore, similar to previous work [15], the 800-nm laser beam before the second chamber has a near-Gaussian profile, which will result in a change of the amount of molecular alignment in the plane perpendicular to the propagation direction. The spatial gradient of the refraction index during rotational revivals will guide the N_2^+ lasing radiation propagating along the channel of rotational wave packets. The guiding effect probably further promotes the interaction of N_2^+ lasing with the Raman-active medium. In addition, it is noteworthy that Raman shifts do not reach saturation with the highest pump energy, a maximum gas pressure, and the longest interaction length available in our experiment. Therefore, Raman scattering can be further extended to a higher order by employing a stronger pump laser, a looser focusing geometry, and a higher gas pressure. We also performed the same measurement in O_2 gas. The maximum Raman shift in the 1-atm O_2 gas is close to the result in the CO_2 gas, indicating that the maximum shift could be robust on the gas species.

To conclude, we have demonstrated the generation of cascaded rotational Raman scattering as high as the 58th order by the interaction of N_2^+ lasing radiation with impulsively excited CO_2 molecules. The Raman scattering spectrum is composed of more than 600 Raman sidebands, which naturally corresponds to a femtosecond pulse train in the temporal domain. Experimental and theoretical analyses reveal that such high-order cascaded Raman scattering is attributed to the specific temporal and spatial characteristics of N_2^+ lasing. These inherent characteristics allow for a good spatiotemporal coupling between the preexcited molecular wave packets and probe pulses. This work opens promising applications of air lasing on ultrafast nonlinear spectroscopy.

This work is supported by the National Key Research and Development Program of China (Grant No. 2018YFB0504400), the National Natural Science Foundation of China (Grants No. 11822410, No. 11734009, and No. 61575211), the Strategic Priority Research Program of Chinese Academy of Sciences (Grant No. XDB16030300), the Key Research Program of Frontier Sciences of Chinese Academy of Sciences (Grant No. QYZDJ-SSW-SLH010), the Key Project of the Shanghai Science and Technology Committee (Grant No. 18DZ1112700), the Shanghai Rising-Star Program (Grant No. 17QA1404600), and the Youth Innovation Promotion Association of Chinese Academy of Sciences (Grant No. 2018284).

[1] S. Baker, I. A. Walmsley, J. W. G. Tisch, and J. P. Marangos, Nat. Photonics **5**, 664 (2011).
[2] H. S. Chan, Z. M. Hsieh, W. H. Liang, A. H. Kung, C. K. Lee, C. J. Lai, R. P. Pan, and L. H. Peng, Science **331**, 1165 (2011).
[3] S. E. Harris and A. V. Sokolov, Phys. Rev. Lett. **81**, 2894 (1998).
[4] A. V. Sokolov, D. R. Walker, D. D. Yavuz, G. Y. Yin, and S. E. Harris, Phys. Rev. Lett. **87**, 033402 (2001).
[5] F. Couny, F. Benabid, P. J. Roberts, P. S. Light, and M. G. Raymer, Science **318**, 1118 (2007).
[6] P. Hosseini, A. Abdolvand, and P. S. J. Russell, Opt. Lett. **41**, 5543 (2016).
[7] A. M. Weiner, Opt. Commun. **284**, 3669 (2011).
[8] V. Torres-Company and A. M. Weiner, Laser Photonics Rev. **8**, 368 (2014).
[9] F. Krausz and M. Ivanov, Rev. Mod. Phys. **81**, 163 (2009).
[10] N. Zhavoronkov and G. Korn, Phys. Rev. Lett. **88**, 203901 (2002).
[11] D. D. Yavuz, D. R. Walker, M. Y. Shverdin, G. Y. Yin, and S. E. Harris, Phys. Rev. Lett. **91**, 233602 (2003).
[12] R. A. Bartels, T. C. Weinacht, N. Wagner, M. Baertschy, C. H. Greene, M. M. Murnane, and H. C. Kapteyn, Phys. Rev. Lett. **88**, 013903 (2002).
[13] M. Wittmann, A. Nazarkin, and G. Korn, Opt. Lett. **26**, 298 (2001).
[14] H. Stapelfeldt and T. Seideman, Rev. Mod. Phys. **75**, 543 (2003).
[15] F. Calegari, C. Vozzi, S. Gasilov, E. Benedetti, G. Sansone, M. Nisoli, S. De Silvestri, and S. Stagira, Phys. Rev. Lett. **100**, 123006 (2008).
[16] S. Varma, Y.-H. Chen, and H. M. Milchberg, Phys. Rev. Lett. **101**, 205001 (2008).
[17] D. Pestov, R. K. Murawski, G. O. Ariunbold, X. Wang, M. Zhi, A. V. Sokolov, V. A. Sautenkov, Y. V. Rostovtsev, A. Dogariu, Y. Huang, and M. O. Scully, Science **316**, 265 (2007).
[18] S. P. Kearney, Combust. Flame **162**, 1748 (2015).
[19] H. U. Stauffer, J. D. Miller, S. Roy, J. R. Gord, and T. R. Meyer, J. Chem. Phys. **136**, 111101 (2012).
[20] J. Yao, G. Li, C. Jing, B. Zeng, W. Chu, J. Ni, H. Zhang, H. Xie, C. Zhang, H. Li, H. Xu, S. L. Chin, Y. Cheng, and Z. Xu, New J. Phys. **15**, 023046 (2013).
[21] B. Xu, J. Yao, Y. Wan, J. Chen, Z. Liu, F. Zhang, W. Chu, and Y. Cheng, Opt. Express **27**, 18262 (2019).
[22] G. Li, C. Jing, B. Zeng, H. Xie, J. Yao, W. Chu, J. Ni, H. Zhang, H. Xu, Y. Cheng, and Z. Xu, Phys. Rev. A **89**, 033833 (2014).
[23] Y. Liu, P. Ding, G. Lambert, A. Houard, V. Tikhonchuk, and A. Mysyrowicz, Phys. Rev. Lett. **115**, 133203 (2015).
[24] G. Herzberg and L. Herzberg, J. Opt. Soc. Am. **43**, 1037 (1953).
[25] M. N. Slipchenko, B. D. Prince, S. C. Ducatman, and H. U. Stauffer, J. Phys. Chem. A **113**, 135 (2009).
[26] J. D. Miller, S. Roy, M. N. Slipchenko, J. R. Gord, and T. R. Meyer, Opt. Express **19**, 15627 (2011).
[27] L. Martinsson, P. E. Bengtsson, M. Aldén, S. Kröll, and J. Bonamy, J. Chem. Phys. **99**, 2466 (1993).